

# Earth and Space Science



## RESEARCH ARTICLE

10.1029/2021EA001834

### Key Points:

- Hydrated Ca-sulfates contain important information of their formation environments on Mars
- Optical constants of gypsum and bassanite are derived through visible/near-infrared to mid-infrared wavelengths
- These optical constants can be used to determine the composition abundances based on radiative transfer theory from remote sensing spectroscopy

### Correspondence to:

E. C. Sklute,  
[ecsklute@psi.edu](mailto:ecsklute@psi.edu)

### Citation:

Ye, C., Sklute, E. C., & Glotch, T. D. (2021). Orientation averaged visible/near-infrared and mid-infrared optical constants of hydrous Ca-sulfates: Gypsum and bassanite. *Earth and Space Science*, 8, e2021EA001834. <https://doi.org/10.1029/2021EA001834>

Received 3 MAY 2021

Accepted 8 SEP 2021

© 2021 The Authors. Earth and Space Science published by Wiley Periodicals LLC on behalf of American Geophysical Union. This is an open access article under the terms of the [Creative Commons Attribution License](https://creativecommons.org/licenses/by/4.0/), which permits use, distribution and reproduction in any medium, provided the original work is properly cited.

## Orientation Averaged Visible/Near-Infrared and Mid-Infrared Optical Constants of Hydrous Ca-Sulfates: Gypsum and Bassanite

Cheng Ye<sup>1,2</sup> , Elizabeth C. Sklute<sup>3</sup> , and Timothy D. Glotch<sup>1</sup> 

<sup>1</sup>Department of Geosciences, Stony Brook University, Stony Brook, NY, USA, <sup>2</sup>Department of Astronomy and Planetary Science, Northern Arizona University, Flagstaff, AZ, USA, <sup>3</sup>Planetary Science Institute, Tucson, AZ, USA

**Abstract** The hydrous Ca-sulfates, gypsum and bassanite, have been detected on Mars using both visible/near-infrared (VNIR) remote sensing measurements and in-situ rover-based mineralogical measurements. Understanding the distributions and abundances of minerals on the Martian surface from remote sensing data is important in evaluating ancient Martian environments. Optical constants are critical input parameters in radiative transfer theory, which allows for the extraction of mineral abundances from a mixture spectrum. We have derived VNIR (0.35–2.5  $\mu\text{m}$ , at 10 nm spectral sampling) optical constants of gypsum and bassanite powders using radiative transfer theory and laboratory reflectance spectra of separated size fractions as well as multiple phase angles. In addition, the MIR (2.5–25  $\mu\text{m}$ , or 4,000–400  $\text{cm}^{-1}$ , at 2  $\text{cm}^{-1}$  spectral sampling) orientation averaged optical constants of gypsum and bassanite were generated using the classical Lorentz-Lorenz dispersion theory. We compare the optical constants of gypsum derived in this work with previously published estimates and note both similarities and differences. The optical constants derived in this work will assist in modeling VNIR reflectance spectra and quantifying mineral abundances from mineral mixtures.

### 1. Introduction

Gypsum ( $\text{CaSO}_4 \cdot 2\text{H}_2\text{O}$ ) and bassanite ( $\text{CaSO}_4 \cdot 0.5\text{H}_2\text{O}$ ) are the most common varieties of hydrous Ca-sulfate minerals (Alpers et al., 2000) and have been found in several regions on Mars by orbital and in-situ observations. Gypsum has been identified in Olympia Planitia in the north polar region and at lower latitudes in Valles Marineris using visible/near-infrared (VNIR) hyperspectral imaging by the Mars Express Observatoire pour la Mineralogie, l'Eau, les Glaces et l'Activite (OMEGA) (Gendrin et al., 2005; Langevin et al., 2005), and in Iani Chaos and Noctis Labyrinthus by the Mars Reconnaissance Orbiter Compact Reconnaissance Imaging Spectrometer for Mars (CRISM) (Sefton-Nash et al., 2012; Weitz et al., 2013, 2015). Bassanite has been found at Mawrth Valles by CRISM (Wray et al., 2010). The possible presence of bassanite in one Chasma of the Noctis Labyrinthus region on Mars from CRISM data has also been discussed by Mangold et al. (2010). Gypsum in veins has been identified in situ at Endeavor crater by Pancam onboard Mars Exploration Rover Opportunity (Squyres et al., 2012). More recently, a variety of Ca-sulfate veins, signifying gypsum and bassanite have been found at Gale crater using several instruments available on Curiosity (e.g., L'Haridon et al., 2018; Nachon et al., 2014, 2017; Rampe et al., 2017; Rapin et al., 2016; Vaniman et al., 2018).

Since gypsum and bassanite formation require the availability of water, the presence of Ca-sulfate minerals can hold important information about aqueous activity throughout Martian history, particularly during the Hesperian period, or “Theiikian” during which massive sulfates on Mars were deposited (Bibring et al., 2006). Gypsum is the first sulfate mineral to precipitate from the evaporite environments on Earth due to its low solubility (Harvie et al., 1984). Formation and stability of bassanite from precipitation is less frequent, and the most common appearances of bassanite on Earth are formed by the dehydration of gypsum in warmer environments (Mees, 1998). However, the formation of bassanite from dehydration of gypsum seems unlikely under current Martian conditions as suggested by Robertson and Bish (2013). The hydration state difference between gypsum and bassanite suggests restricted environmental conditions where water is present with different temperatures, humidity, and pH levels for the formation of each mineral. Generally, gypsum forms at a temperature lower than 60°C at neutral pH, while bassanite forms at a higher temperature between 80°C and 120°C at pH 8–9 with a low water activity (Bishop et al., 2014; Osso-

rio et al., 2014). When extrapolating laboratory dehydration/rehydration experiments on  $\text{CaSO}_4 \cdot n\text{H}_2\text{O}$  to Mars-relevant surface conditions, the presence of gypsum indicates a hydrating environment at relatively low temperatures, while gypsum dehydration to bassanite is restricted to local areas at high temperatures associated with impact/volcanic events (Robertson & Bish, 2013). To better clarify the details of these aqueous environments, it is necessary to constrain the exact type and abundance of Ca-sulfate minerals present on the Martian surface. Although Mars landers and rovers can provide comprehensive information on these minerals to unravel the formation environments, they are limited to local regions. Qualitative identification and quantitative extraction of the type and abundance of minerals on the surface from broader regional remote sensing data is critical to shedding light on a complete view of ancient Martian environments.

VNIR reflectance spectroscopy is one of the most important and useful methods to identify minerals from a remote sensing platform. Beyond qualitative mineral identification, it is often highly desirable to place quantitative constraints on the abundances of single minerals present in a mixture for further analysis of the ancient formation environment. Spectral deconvolution techniques in the mid-infrared (MIR) and VNIR differ. Generally, spectra of coarse particulates ( $>60 \mu\text{m}$ ) can be modeled via a linear combination of individual minerals weighted by their areal abundances primarily at MIR wavelengths because the light is commonly absorbed before it can scatter multiple times (e.g., Ramsey & Christensen, 1998). However, in the VNIR wavelength region, determining the quantitative abundances of single minerals in a mixture is difficult because spectral response does not mix linearly with abundance. This is because light generally reflects multiple times in an intimately mixed medium before reaching the detector (Hapke, 2012).

Radiative transfer theory (Chandrasekhar, 1960), which describes the interaction of light with a particulate medium, can be used to address the problem of nonlinear spectral mixing of intimate mixtures and to extract quantitative mineral contents. An approach derived from radiative transfer theory widely used in planetary studies is Hapke's bidirectional reflectance model (Hapke, 1981, 2012). In Hapke's model, a reflectance spectrum can be computed as a function of single-scattering albedo, illumination and viewing angles, and scattering phase function. Although reflectance is not linearly correlated with concentrations in a mixed spectrum, the single scattering albedos of individual components in a mixture do combine linearly. Single scattering albedo or the probability that a photon interacting with a particle will be scattered rather than absorbed, is a function of the material's complex index of refraction, also termed optical constants, and particle size. Optical constants ( $n$  and  $k$ , real and imaginary parts of the complex index of refraction, respectively), are the fundamental optical properties of minerals and are independent of particle size and shape. The details of light-matter interaction for minerals are related to their optical constants. At MIR wavelengths, where both  $n$  and  $k$  are large and vary substantially with wavelength, both play a strong role in the shape and magnitude of reflectance or emission spectral features. The large  $k$ -values found in this wavelength region cause light to typically be absorbed by the first particle interaction, causing the linear mixing behavior for coarse particulates described above (Adams 1993; Gillespie, 1992). At VNIR wavelengths, the shapes and depths of spectral absorption features are primarily controlled by the imaginary part of the index of refraction,  $k$ . While  $n$  does not vary substantially at VNIR wavelengths, knowing its absolute value at each wavelength is important to accurately model nonlinear spectral mixing. Therefore, optical constants are important input parameters in a radiative transfer calculation to extract mineral abundances from VNIR remote sensing spectroscopy.

Optical constants are not available for a variety of major rock-forming minerals or exist only for a few compositions (Lukey, 1998). There are various approaches to modeling the optical constants of minerals. Classical dispersion theory is widely used to derive optical constants of orthorhombic and higher symmetric minerals in the MIR region (Glotch et al., 2007; Glotch & Rossman, 2009; Roush et al., 1991; Roush, 1995, 1996; Spitzer & Kleinman, 1961). Anisotropic crystals have quite different optical properties depending on their crystallographic orientation. Spectra of these minerals must be measured at multiple crystallographic orientations using polarized light to properly define their optical constants (Arnold et al., 2014; Aronson et al., 1983, 1985; Mayerhöfer & Popp, 2007; Ye, Rucks, et al., 2019). At wavelengths  $<5 \mu\text{m}$ , the assumption that Fresnel reflectivity is the dominant source of reflected light becomes increasingly invalid due to a decrease in the imaginary index of refraction, which results in an increasing contribution of multiply scattered light (Roush et al., 1991). Therefore, classical dispersion theory can only be properly utilized in the MIR regime. Optical constants derived from transmission measurements have also been performed by Roush

et al. (2007). This method requires a sample to be made into thin films or to occur as pure transparent single crystals, which are not available for a variety of minerals.

Radiative transfer theory methods can be used to derive bulk, orientation-averaged optical constants for powdered materials (Hapke, 1981; Shkuratov et al., 1999). Since sample preparation for powders is inexpensive and convenient compared to other techniques mentioned above, deriving optical constants from diffuse reflectance of powders is widely used. Lucey (1998) used Hapke's model to derive the imaginary refractive index,  $k$ , of olivine and pyroxene from reflectance spectra with a series of fixed initial assumptions for parameters in Hapke's formulation, including a constant real part of the refractive index,  $n$ . Roush (2003, 2005) described an additional iterative approach that allows determination of  $n$  as a function of wavelength using a subtractive Kramers–Kronig analysis. Dalton and Pitman (2012), Pitman et al. (2014), Roush et al. (2007), and Roush (2021) combined Hapke's theory and subtractive Kramers–Kronig analysis to determine optical constants through a few iterations. In those works, the typical optical constants they derived are particle size dependent. However, optical constants should be independent of particle size, so those results must be due to the simplifications inherent in their chosen radiative transfer approach. In order to eliminate the particle size effect, they iteratively adjusted the grain size to converge the deviation of  $k$  to the mean, or averaged the  $k$ -values for multiple grain sizes (e.g., Lucey, 1998; Roush et al., 2007).

Sklute et al. (2015) slightly modified this method to determine optical constants of several compositions of the  $\text{Fe}^{3+}$  sulfate, jarosite. They used a global optimization algorithm to determine the particle size-independent  $k$ . They also derived the MIR  $k$  through classical dispersion theory and combined it with the VNIR  $k$  to create a larger wavelength range over which to determine the real part of the index of refraction,  $n$ , using Kramers–Kronig analysis. They showed that including the longer wavelength  $k$ -values in their calculations had a strong effect on the VNIR values of  $n$ . The method from Sklute et al. (2015) not only provided a robust way to derive wavelength-dependent optical constants but also made an appropriate constraint on the phase function. One of the widely used approximations for phase function in Hapke's model is a two-term Legendre polynomial. In previous works, authors used constant coefficients for the Legendre polynomial (e.g., Lucey, 1998; Pitman et al., 2014; Robertson et al., 2016), while Sklute et al. (2015) found the wavelength-dependent Legendre polynomial coefficients by fitting spectra acquired at 7 different phase angles for each particle size. However, the method from Sklute et al. (2015) solved for too many variables (the Legendre polynomial coefficients  $b$  and  $c$ , effective particle size  $\langle D \rangle$ , internal scattering coefficient  $s$ , and imaginary refractive index  $k$ ) at the same time. This can lead to a non-unique solution, many of which might not be physically reasonable. In this work, we apply the modeling procedure of Sklute et al. (2021), which made an improved modification to the method of Sklute et al. (2015), to separate the derivation of phase function and  $k$  values. The details of the modeling method are presented in Section 3.3.

In this work, we derive the orientation averaged optical constants of gypsum and bassanite in the MIR wavelength range using classical dispersion theory (e.g., Glotch et al., 2007; Glotch & Rossman, 2009) and in the VNIR wavelength range following the method of Sklute et al. (2015, 2021). Unlike most previous studies, this work determines grain size independent  $k$ -values along with the wavelength-dependent phase function and  $n$  values based on careful laboratory measurements and rigorous theory in the VNIR region. Optical constants of gypsum have been determined by Roush et al. (2007) and Robertson et al. (2016). To our knowledge, however, there are no optical constants available for bassanite. Therefore, this work not only can be used as a direct comparison to the past efforts but also is an extension of available mineral optical constants.

## 2. Background Theory

### 2.1. Hapke Model

Hapke's radiative transfer model is used in this study to derive optical constants. In this work, we use a calibrated Spectralon standard, which we assume is a Lambertian scatterer. Following these assumptions, the radiance coefficient in Hapke's bidirectional reflectance model (Hapke, 1981) is:

$$REFF(i, e, g) = \frac{w}{4} \frac{1}{\mu_0 + \mu} \left\{ [1 + B(g)] P(g) + H(\mu_0) H(\mu) - 1 \right\}. \quad (1)$$

In Equation 1  $\mu_0 = \cos(i)$  and  $\mu = \cos(e)$ , where  $i$  and  $e$  are the incidence angle and emergence angle of light, respectively, and  $g$  is the phase angle, where  $g = i + e$ . The backscattering function  $B(g)$  can be set to zero for the purpose of this work since the phase angles are greater than  $15^\circ$  (Mustard & Pieters, 1989).

The single scattering phase function  $P(g)$  can be approximated by a two-term Legendre polynomial of the following form:

$$P(g) = 1 + b * \cos(g) + c * [1.5\cos^2(g) - 0.5], \quad (2)$$

where phase function coefficient  $b$  describes the degree of forward/backward scattering, and coefficient  $c$  characterizes the degree of side scattering (Mustard & Pieters, 1989).

The parameter  $w$  is the single scattering albedo, defined as  $w = \frac{Q_s}{Q_e}$ , where  $Q_s$  and  $Q_e$  are the scattering and extinction efficiency of a particle, respectively. For closely packed particles,  $Q_e = 1$ , so

$$w \cong Q_s = S_e + (1 - S_e) \frac{1 - S_i}{1 - S_i \Theta}. \quad (3)$$

$S_e$  is the Fresnel surface reflection coefficient for externally incident light,  $S_i$  is the Fresnel reflection coefficient for internally scattered light. They can be approximated by

$$S_e = \frac{(n-1)^2 + k^2}{(n+1)^2 + k^2} + 0.05. \quad (4)$$

$$S_i = 1.014 - \frac{4}{n(n+1)^2}. \quad (5)$$

$\Theta$  is the internal transmission factor and is given by

$$\Theta = \frac{r_i + \exp(-\sqrt{\alpha(\alpha+s)\langle D \rangle})}{1 + r_i \exp(-\sqrt{\alpha(\alpha+s)\langle D \rangle})}. \quad (6)$$

Here,  $r_i$  is the bihemispherical reflectance of a semi-infinite medium and is given by

$$r_i = \frac{1 - \left[ \frac{\alpha}{(\alpha+s)} \right]^{\frac{1}{2}}}{1 + \left[ \frac{\alpha}{(\alpha+s)} \right]^{\frac{1}{2}}}, \quad (7)$$

where  $\alpha$  is the absorption coefficient, such that

$$\alpha = \frac{4\pi k}{\lambda}. \quad (8)$$

$s$  is an internal scattering coefficient and  $\langle D \rangle$  is the effective grain size, or optical path length (Hapke, 2001, 2012, 2012; Pieters et al., 1993). We should note that the term  $\langle D \rangle$  is different from the physical grain size of a particle.

Finally, Chandrasekhar's isotropic  $H$ -function can be extrapolated from a lookup table of  $\mu$ ,  $w$ , and  $H(x)$  from Chandrasekhar (1960) or approximated after Hapke (2012) as

$$H(x) = \left\{ 1 - wx \left[ r_0 + \frac{1 - 2r_0x}{2} \ln \left( \frac{1+x}{x} \right) \right] \right\}^{-1} \quad (9)$$

where the variable  $r_0 = (1 - \sqrt{1-w}) / (1 + \sqrt{1+w})$ . When single scattering albedo is very close to 1, which is the case for our sample at short wavelength, the approximate solution of  $H$ -function shows large disagree-

ment with the exact solution of  $H$ -function (Hapke, 2012). Therefore, we use the extrapolation of Chandrasekhar's  $H$ -function table as  $H(x)$  in Hapke's model.

## 2.2. Singly Subtractive Kramers–Kronig Analysis

A single subtractive Kramers–Kronig analysis derives  $n$  as a function of wavelength from existing values of  $k$  (Lucarini et al., 2005). The Kramers–Kronig equations are a general class of expressions that relate the real and imaginary components of any complex response function that is analytic in the half-plane above the  $X$ -axis in a Cartesian coordinate system. Formal Kramers–Kronig analysis requires data at all wavelengths, which is a criterion that can never be met. However, a subclass of these expressions, singly subtractive Kramers–Kronig relations, are useful for limited spectral ranges. Therefore, we used MIR  $k$ -values determined from classical dispersion theory to extend the range for a more convergent solution. The singly subtractive Kramers–Kronig transformation can be written as

$$n(\nu) = n_0 + \frac{2(\nu^2 - \nu_0^2)}{\pi} P \int_0^\infty \frac{\nu' k(\nu')}{(\nu^2 - \nu'^2)(\nu'^2 - \nu_0^2)} d\nu', \quad (10)$$

where  $n(\nu)$  is the real refractive index at frequency  $\nu$ , and  $n_0$  is a known value for the index of refraction at point  $\nu_0$  (frequency at sodium D line 0.58929  $\mu\text{m}$ ).  $\nu'$  is a dummy variable of integration.  $P$  denotes the Cauchy principal value of the integral.

## 2.3. Dispersion Theory

To estimate the MIR optical constants, classical dispersion theory in combination with Fresnel equations are used in this study following the method of Spitzer and Kleinman (1961). Dispersion theory describes the vibration of a crystal lattice as a collection of harmonic oscillators. Each lattice oscillator is defined by a set of dispersion parameters, including resonant frequency ( $\nu$ ), band strength ( $4\pi\rho$ ), and band width ( $\gamma$ ). The optical constants are related to these oscillator parameters as follows:

$$n^2 - k^2 = \varepsilon_0 + \sum_j \frac{4\pi\rho_j \nu_j^2 (\nu_j^2 - \nu^2)}{(\nu_j^2 - \nu^2)^2 + (\gamma_j^2 \nu_j^2 \nu^2)} \quad (11)$$

$$nk = \sum_j \frac{4\pi\rho_j \nu_j^2 (\gamma_j \nu_j \nu)}{(\nu_j^2 - \nu^2)^2 + (\gamma_j^2 \nu_j^2 \nu^2)} \quad (12)$$

where  $\varepsilon_0$  is the high frequency dielectric constant,  $j$  represents the  $j$ th oscillator.

The total reflectance can then be calculated using optical constants through Fresnel equations:

$$R_T = \frac{R_\perp^2 + R_\parallel^2}{2} \quad (13)$$

$$R_\parallel^2 = \frac{(\cos \theta - u)^2 + v^2}{(\cos \theta + u)^2 + v^2} \quad (14)$$

$$R_\perp^2 = \frac{\left[ (n^2 - k^2) \cos \theta - u \right]^2 + (2nk \cos \theta - v)^2}{\left[ (n^2 - k^2) \cos \theta + u \right]^2 + (2nk \cos \theta + v)^2} \quad (15)$$

$$u = \left( \frac{n^2 - k^2 - \sin^2 \theta + \left[ (n^2 - k^2 - \sin^2 \theta)^2 + 4n^2 k^2 \right]^{1/2}}{2} \right)^{1/2} \quad (16)$$

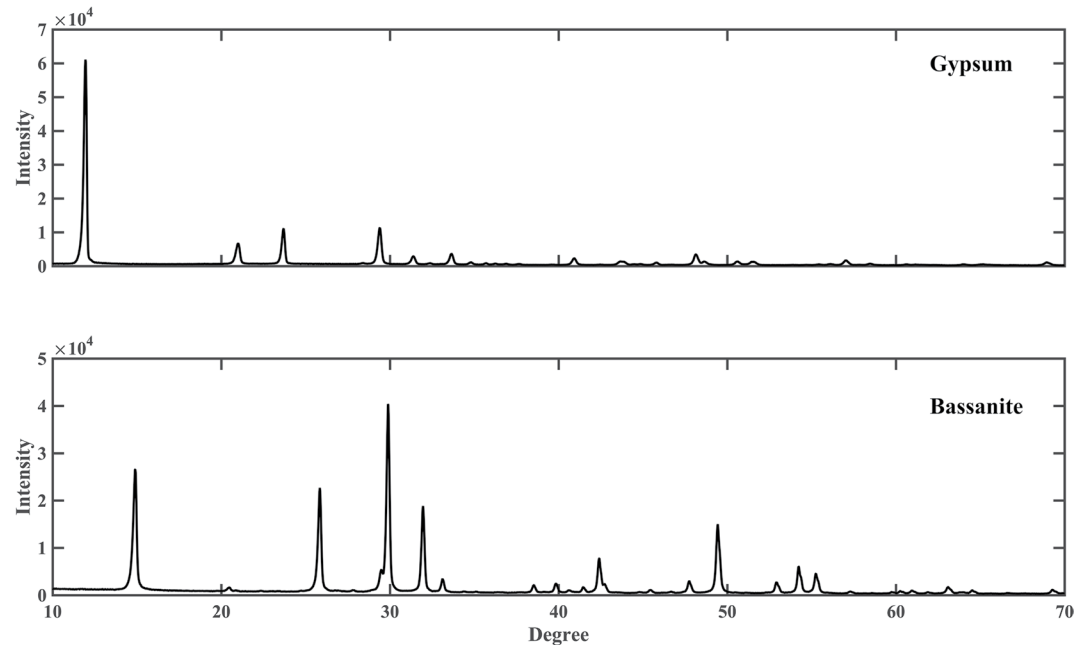


**Figure 1.** XRD patterns for gypsum and bassanite.

$$v = \left( \frac{-\left(n^2 - k^2 - \sin^2\theta\right) + \left[\left(n^2 - k^2 - \sin^2\theta\right)^2 + 4n^2k^2\right]^{1/2}}{2} \right)^{1/2} \quad (17)$$

where  $\theta$  is the incident angle.

### 3. Method

#### 3.1. Sample Description and Preparation

The chunk gypsum sample was purchased from Ward's Science. Bassanite was synthesized by putting powdered gypsum in an oven at 80°C overnight. Powder X-ray diffraction (XRD) patterns were collected using the Rigaku Miniflex X-ray diffractometer to determine the purity of phase in the Department of Geosciences, Stony Brook University. The instrument was operated in the Bragg-Brentano geometry configuration with CuK $\alpha$  radiation (1.54 Å) and D/teX Ultra 1D detector. The patterns were obtained at a scanning rate of 0.5° per minute with a 0.02° step size from 10° to 70° for these two minerals (Figure 1). XRD patterns of both our samples are consistent with those of pure samples from the Caltech RRUFF database. Gypsum and bassanite were ground and sieved into four size fractions (<32, 90–125, 125–180, 180–250  $\mu\text{m}$ ). Samples were washed with ethanol to remove clinging fines. The smallest size fraction of gypsum and bassanite was pressed into compact pellets  $\sim$ 2 mm thickness and 13 mm diameter providing a smooth surface like a mirror for MIR specular reflectance measurements.

#### 3.2. Laboratory Measurements

VNIR (0.35–2.5  $\mu\text{m}$ ) reflectance spectra were acquired at 7 phase angles from 45° to 105° (we fixed the incident angle  $i = 45^\circ$ , and changed the viewing angle  $e = 0^\circ, -10^\circ, -20^\circ, -30^\circ, -40^\circ, -50^\circ, -60^\circ$ ) for each sample referenced to a square calibrated Spectralon standard under identical conditions using ASD Fieldspec3 spectroradiometer at Stony Brook University's Center for Planetary Exploration (CPEX). The instrument consists of 512 element silicon photodiode array detectors over the 350–1,000 nm range with a spectral sampling of 1.4 nm and two TE cooled InGaAs photodiode detectors (SWIR1: 1,000–1,830 nm; SWIR2: 1,830–2,500 nm) over the 1,000–2,500 nm range with a spectral sampling of 2 nm. All spectra were resampled to 1 nm spectral

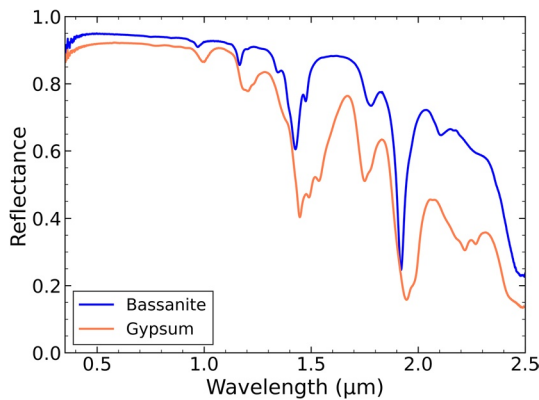


**Figure 2.** Example laboratory visible/near-infrared reflectance spectra of gypsum and bassanite measured with  $>250 \mu\text{m}$  particle size used in this study. Incidence and emergence angles were  $30^\circ$  and  $0^\circ$ , leading to a phase angle of  $30^\circ$  for these measurements.

sampling with the provided software. Designed phase angles were achieved by using a custom-built goniometer with the angular error of  $<2^\circ$  (Skulte et al., 2015). Each spectrum was collected with an average of 300 scans to provide a sufficient signal-to-noise ratio. Each sample was run four times, rotating sample cup  $90^\circ$  every time, and then all spectra were averaged to produce the final spectrum. The detector was optimized with the change of phase angle, and white reflectance (300 scans dark current, 600 scans white reference) was collected before each measurement. During the spectral measurements, the viewing spot size would become more elliptical at larger phase angles. In order to avoid the detector viewing areas outside the sample, an  $8^\circ$  field of view foreoptic lens was attached to the detector and sample cups were placed close to the foreoptic. All reflectance spectra were calibrated to correct the photometric effect of the Spectralon according to the method of Yang et al. (2019).

VNIR reflectance spectra of gypsum and bassanite are dominated by absorption features caused by combinations and/or overtones of  $\text{H}_2\text{O}$  vibrational modes, and the individual wavelength of each of these features in gypsum and bassanite spectra have been presented and analyzed in

previous studies (Bishop et al., 2014; Cloutis et al., 2006, 2008; Crowley, 1991; Harrison, 2012; Hunt, 1977). The VNIR reflectance spectrum of gypsum exhibits bands at 1.0, 1.2, 1.4–1.5, 1.75, 1.9–2.0, 2.2, and  $2.4 \mu\text{m}$ . Although bassanite spectra have similar spectral features to gypsum, there are adequate differences to distinguish these two minerals. Characteristic bands at 1.0, 1.2,  $\sim 1.4$ ,  $\sim 1.9 \mu\text{m}$  in bassanite are narrower and shifted to shorter wavelengths compared to the bands in gypsum spectra. The absorption band at  $2.2 \mu\text{m}$  in gypsum is not seen in bassanite, but a band at  $\sim 2.1 \mu\text{m}$  is present in bassanite, but not in gypsum (Figure 2).

MIR specular reflectance spectra were collected for each pellet referenced to a gold mirror using a Nicolet 6700 FTIR spectrometer in CPEX with an equipped specular reflectance accessory with  $30^\circ$  incidence and emergence angles. The spectrometer is equipped with a deuterated L-alanine doped triglycine sulphate (DLATGS) detector and a CsI beamsplitter and uses a dry air purge to reduce contributions from atmospheric  $\text{CO}_2$  gas and  $\text{H}_2\text{O}$  vapor. The MIR spectra of each sample were acquired from  $400\text{--}4,000 \text{ cm}^{-1}$  at  $2 \text{ cm}^{-1}$  spectral sampling with a total of 512 scans.

### 3.3. Computation Procedure

This work is based on the procedure from Skulte et al. (2021) to limit the potential of deriving non-unique solutions. Here, we summarize the modeling method.

The optical constants  $n$  and  $k$  were calculated using Hapke's model of radiative transfer theory through several steps of minimization (Figure 3) using a MATLAB encoded routine. First, reflectance spectra for each grain size at one phase angle were converted to an initial guess for single scattering albedo,  $w$ , by setting

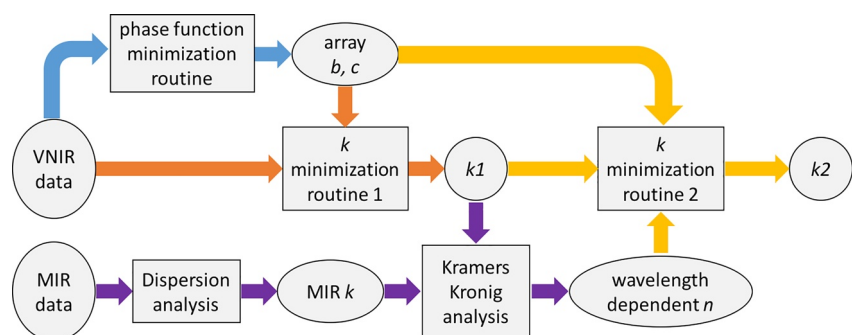


**Figure 3.** Flow chart of visible/near-infrared optical constants calculations performed in this work. Step 1: Blue arrows; Step 2: Orange arrows; Step 3: Purple arrows; Step 4: Yellow arrows.

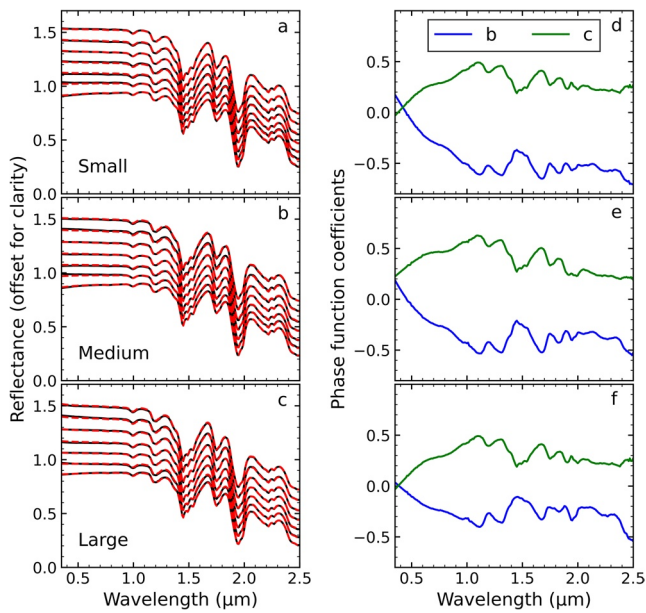


**Figure 4.** Modeled and measured reflectance for three sizes at seven phase angles for gypsum. (a) shows the small grain size (90–125 μm) spectra, (c) shows the medium grain size (125–180 μm) spectra, and (e) shows large grain size (180–250 μm) spectra. Spectra from 7 phase angles are offset for clarity (from bottom to top corresponding to  $g = 45^\circ, 55^\circ, 65^\circ, 75^\circ, 85^\circ, 95^\circ, 105^\circ$ ). Determined two-term Legendre polynomial phase function coefficients  $b$  and  $c$  for gypsum. Panel (b) shows the small grain size parameters, (d) shows the medium grain size parameters, and (f) shows the large grain size parameters.

the initial guess for phase function coefficients  $b$  and  $c$  from Mustard and Pieters (1989). The ranges of  $b$  and  $c$  ( $-1.7 < b < 1.7$ ,  $-1 < c < 2$ ) were adopted from Mustard and Pieters (1989). Then, we leverage the fact that all spectral variations due to phase angle and those due to grain size are mathematically separable. According to Equation 1, all phase angles of a given grain size should have the same single scattering albedo. Thus, we can robustly derive phase function parameters by requiring  $w$  for each grain size to remain constant across phase space and forcing phase function coefficients,  $b$  and  $c$ , to account for all spectral variation due to phase angle. This step derives wavelength-dependent  $b$ ,  $c$ , and  $w$  for each grain size using a least squares minimization to simultaneously model each group of the 7 phase angle spectra. The phase functions coefficients for each grain size fraction from this step are used as constants in all following calculations.

Second, a guess for  $k$  is derived from  $w$  using a fixed effective particle size  $\langle D \rangle$  (set as the lowest boundary of the size distribution), as well as an internal scattering coefficient  $s$  (set to zero) for each grain size. Then, a grain-size independent  $k$  is derived by modeling three grain sizes simultaneously using  $b$  and  $c$  from the previous step and requiring all spectral variation due to grain size be accounted for by  $\langle D \rangle$  and  $s$ . Bounds for  $\langle D \rangle$  are allowed to vary between 1/3 the lowest value through the highest value of the sieved size fraction (see Hapke [2012] discussion for equant particles), and  $s$  was allowed to vary between 0 and  $0.1 \mu\text{m}^{-1}$ .

Third, the VNIR  $k$  was combined with MIR (2.5–25 μm)  $k$  calculated from classical dispersion theory for pellets, and this long range  $k$  was used to derive VNIR wavelength-dependent  $n$  by a subtractive Kramers–Kronig analysis.

Finally, we used the new wavelength-dependent  $n$  to run the minimization routine for a new  $k$  and vice versa. The third and fourth steps were iterated several times until  $n$  and  $k$  did not change substantially.

## 4. Results and Discussion

### 4.1. Phase Function

A two-term Legendre polynomial was used as the phase function in this study. A two-term Henyey–Greenstein (2HG) phase function was also tested, but failed to produce reasonable convergence between the model and the data over the full grain size, phase angle, and wavelength range. While the 2HG phase function has been favored by some authors (e.g., Cord et al., 2003; Hartman & Domingue, 1998; McGuire & Hapke, 1995; Shepard & Helfenstein, 2007), we note that those publications focused on one or a handful of wavelengths in the VIS region of the spectrum, whereas we fit hundreds of wavelengths throughout the entire VNIR wavelength range and across all phase space. Furthermore, to our knowledge, phase behavior of sulfates has not been adequately studied, however, Sklute et al. (2015) similarly found a 2HG phase function could not adequately model the jarosite phase data across the full VNIR region.

We derived the wavelength-dependent phase function coefficients  $b$  and  $c$  from 7 phase angles instead of assuming a constant number for them. Figures 4 and 5 show the phase function fitting results between calculated and measured reflectance spectra for 3 sizes at 7 phase angles, as well as final phase function coefficients  $b$  and  $c$  for 3 sizes of gypsum and bassanite, respectively. Figure 6 shows the variation of the modeled phase function of gypsum and bassanite at different grain sizes.

We note that our modeled phase functions for gypsum and bassanite are significantly different from each other. The derived phase function of gypsum represents moderated forward scattering, which is consistent with the assumption for most bright minerals. However, the phase function we modeled for bassanite shows strong backscattering properties. We think the reverse trend of phase scattering behavior for gypsum and

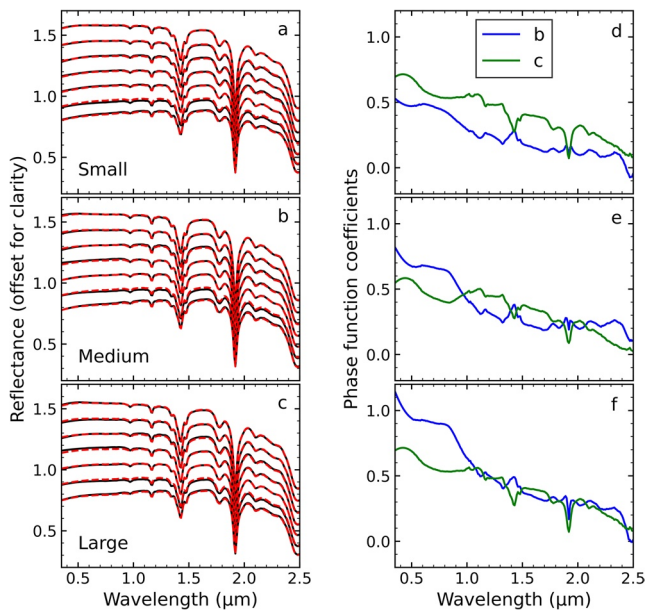


**Figure 5.** Modeled and measured reflectance for three sizes at 7 phase angles for bassanite. (a) shows the small grain size (90–125  $\mu\text{m}$ ) spectra, (c) shows the medium grain size (125–180  $\mu\text{m}$ ) spectra, and (e) shows large grain size (180–250  $\mu\text{m}$ ) spectra. Spectra from 7 phase angles are offset for clarity (from bottom to top corresponding to  $g = 45^\circ, 55^\circ, 65^\circ, 75^\circ, 85^\circ, 95^\circ, 105^\circ$ ). Determined two-term Legendre polynomial phase function coefficients  $b$  and  $c$  for bassanite. (b) shows the small grain size parameters, (d) shows the medium grain size parameters, and (f) shows the large grain size parameters.

bassanite could be caused by several reasons. First, the phase behavior is determined from 7 phase angles ranging from  $45^\circ$  to  $105^\circ$  in this study. This limited range of angles may not be sufficient to appropriately determine phase function with a two-term phase function. However, attempts to restrict  $b$  and  $c$  values to a forward scattering regime led to poor convergence between the data and the fits. Second, bassanite samples are composed of irregular particles, which could create substantial surface roughness and may cause the phase function to display backscattering (Hapke, 2012). Third, high brightness and transparency of bassanite compared to gypsum (higher reflectance of bassanite compared to gypsum measured under the same condition) could make light transport deeper and possibly reach the black sample cup. The backscattering behavior of bassanite is possible partly coming from the combined scattering behavior of the bassanite and the underlying black sample cup. Finally, due to the similar physical properties of bassanite and gypsum, as well as the same experimental and modeling condition, the derived phase functions of bassanite and gypsum may represent their real phase scattering features. If this is true, minerals in the same class could have different phase scattering behavior. Therefore, more caution is warranted when assuming the phase function for different particles in spectral modeling. A broad and comprehensive study of the phase scattering behavior for different rock-forming minerals is worth doing in the future.

#### 4.2. MIR Optical Constants

Non-linear least squares optimization is used to fit the calculated and measured spectra for the optimized oscillator parameters following the method of Glotch et al. (2007). MIR optical constants of gypsum and bassanite derived from classical dispersion theory and Fresnel equations are shown in Figure 7 and the oscillator parameters used to fit the reflectance spectra are shown in Table 1.

#### 4.3. VNIR Optical Constants

The initial constant  $n$  was calculated as the average of the crystallographic axis specific refractive indices at  $0.58929 \mu\text{m}$ , such that  $n_{\text{vis}} = (n_\alpha + n_\beta + n_\gamma)/3$ . The visible refractive indices of gypsum and bassanite for each crystallographic axis (Anthony et al., 1995) and averaged values are listed in Table 2.

The effective particle size,  $\langle D \rangle$ , is the most influential factor that affects the derivation of optical constants. Unlike Lucey (1998) and Roush et al. (2007), who adjusted  $\langle D \rangle$  for each sample to obtain  $k$  suitable for multiple grain sizes, the method used in this work allows for the simultaneous fitting of multiple data sets to determine  $\langle D \rangle$  for each particle size, along with a single array for  $k$ . Derived effective grain size  $\langle D \rangle$  and  $k$  values of gypsum from various initial guesses of  $\langle D \rangle$  are perfectly identical with each other, and results for bassanite are also very close to each other (Figure 8). Therefore, results generated in this work likely represent  $\langle D \rangle$  associated with a global minimum deviation between the model and data, as they are independent of the initial guess  $\langle D \rangle$ . We found that the derived  $\langle D \rangle$  is lower than the bottom of its grain size fraction range. The global optimization routines allow  $\langle D \rangle$  to vary from 1/3 the lowest value to the highest value of the sieved size range because the mean ray path length  $\langle D \rangle$  is usually smaller than the average particle diameter for irregular particles with internal imperfections (Hapke, 2012).

Reflectance spectra in this study were measured at 7 phase angles for each of three-grain size. Each set of reflectance data consists of three-grain sizes at one phase angle, which was used as input for the program to generate one set of optical constants. We can see that the variation of derived  $k$ -values from reflectance data at 7 phase angles is limited to a small range (Figure 9), and the final  $k$ -values are highly sensitive to the associated  $\langle D \rangle$  (Table 3). For example, derived  $k$  values for both gypsum and bassanite at  $g = 75^\circ$  and  $95^\circ$  are smaller than  $k$  values at rest of phase angles, while their corresponding effective grain sizes are larger com-

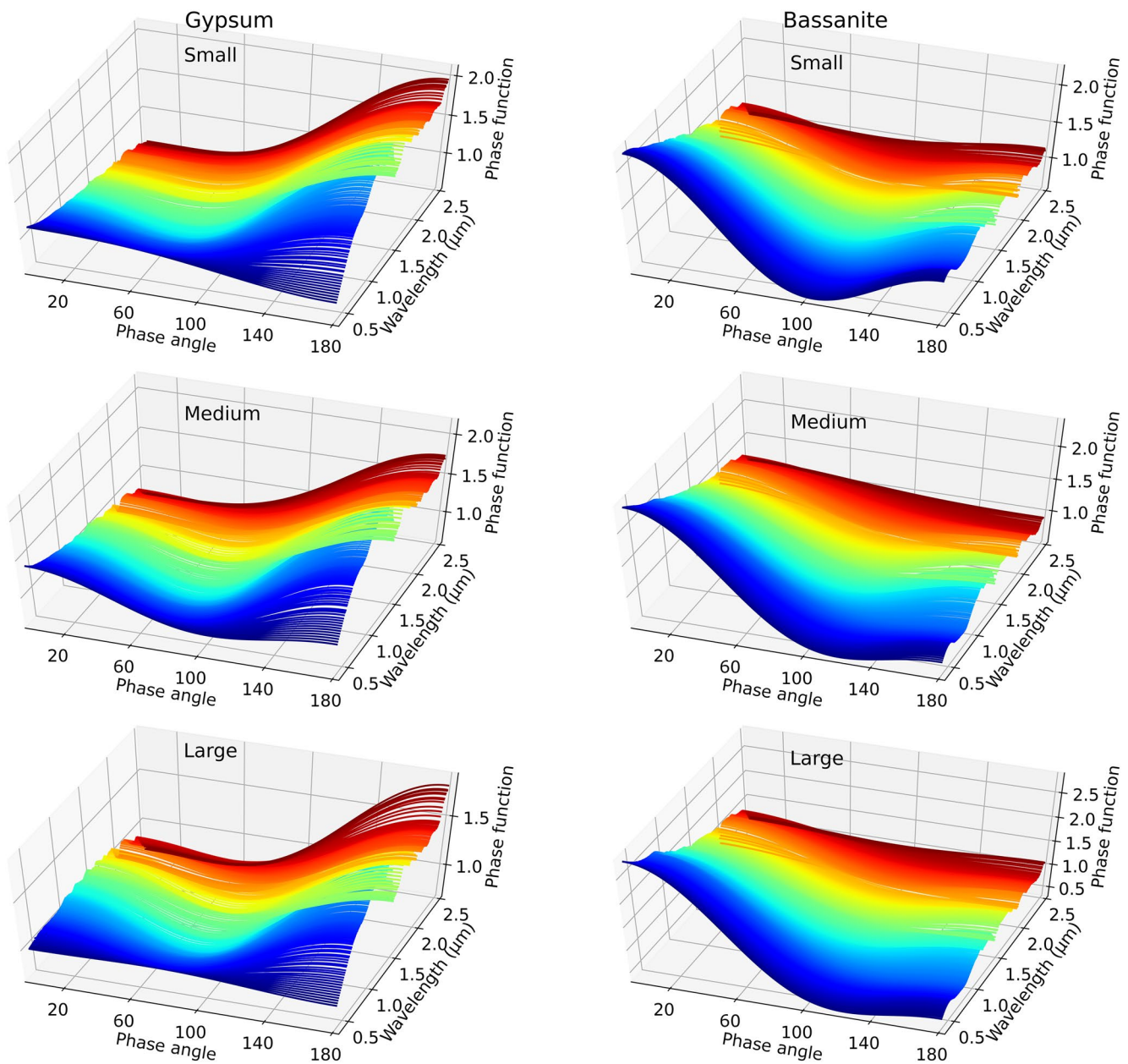


**Figure 6.** Variation of phase function modeled with a two-term Legendre Polynomial for gypsum (left) and bassanite (right) with three different grain sizes (top: small grain size; middle: medium grain size; bottom: large grain size).

pared to others. This is likely due to the uncertainties from the laboratory measurements at these phase angles, which can be partly witnessed from fitting results at phase function derivation step (Figures 4 and 5); spectral fitting results at  $g = 75^\circ$  and  $95^\circ$  are relatively poor compared to others. Ideally, with more accurate laboratory measurements and appropriate acquisition of phase function, derived  $k$  values in this study would be the same for reflectance data at any phase angles. Therefore, the variation of  $k$ -values determined from reflectance data at different phase angles records the uncertainties of our laboratory spectral measurements. In this work, we averaged the derived optical constants from all 7 phase angles as our final results.

In the Hapke model, the parameter  $s$ , the internal scattering efficiency, cannot be known in advance for an individual sample. Hapke and Wells (1981) found the best value of  $s$  of  $600 \text{ cm}^{-1}$  for synthetic silicate glass particles. Lucey (1998) discussed the parameter  $s$  for natural olivine and pyroxene and set  $s$  to zero. Roush

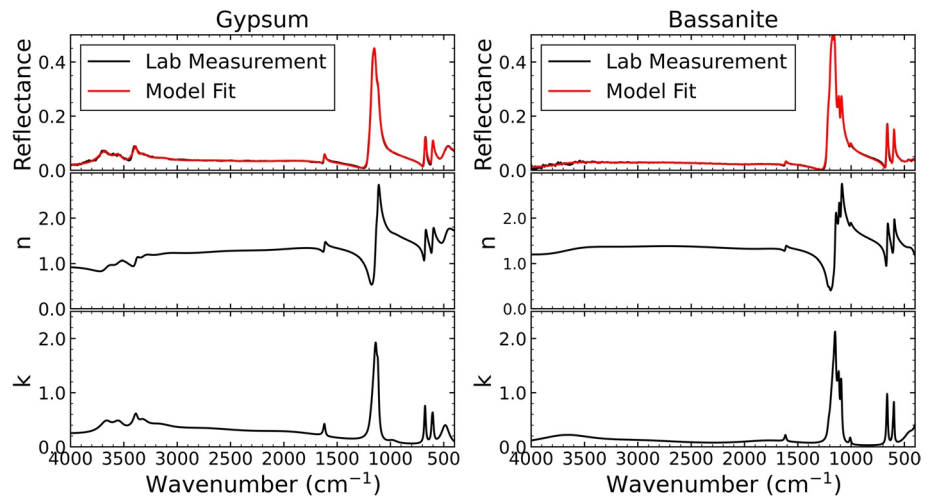


**Figure 7.** Measured and modeled mid-infrared reflectance, and derived optical constants for gypsum (left) and bassanite (right).

et al. (2007) manually varied  $s$  to  $1.25 \text{ cm}^{-1}$  for consistent spectral comparison. In this study, we determined  $s$  along with  $k$  through global minimization routines (Table 3).

Porosity is another important factor in reflectance spectra (Hapke, 2008, 2012). The constant  $K$ , the porosity factor, is

$$K = -\frac{\ln\left(1 - 1.209\phi^{\frac{2}{3}}\right)}{1.209\phi^{\frac{2}{3}}}, \quad (18)$$

**Table 1**  
Oscillator Parameters for Gypsum and Bassanite

Gypsum			Bassanite		
$\varepsilon_0 = 1.1821$			$\varepsilon_0 = 1.7667$		
$\nu$	$\gamma$	$4\pi\rho$	$\nu$	$\gamma$	$4\pi\rho$
482	0.1846	0.2240	339	0.1216	0.7633
601	0.0313	0.0497	456	0.2858	0.1547
609	0.0229	0.0085	597	0.0155	0.0358
673	0.0232	0.0479	605	0.0294	0.0185
979	0.1033	0.0173	660	0.0190	0.0554
1116	0.0193	0.1088	1,008	0.0159	0.0071
1134	0.0254	0.1210	1,091	0.0146	0.0762
1618	0.0131	0.0082	1,114	0.0151	0.0628
1971	0.5355	0.2611	1,127	0.0179	0.0264
2802	0.4358	0.2658	1,146	0.0179	0.1194
3168	0.1126	0.0439	1,167	0.0123	0.0063
3316	0.0372	0.0149	1,181	0.0166	0.0027
3383	0.0133	0.0063	1,206	0.0174	0.0027
3543	0.0345	0.0139	1,615	0.0121	0.0038
3656	0.0333	0.0119	1,789	0.4072	0.1002
4224	0.2714	0.0859	3,013	0.4065	0.0954
			3,665	0.1799	0.0825

**Table 2**  
Visible Refractive Index Values for Gypsum and Bassanite Used as the Initial Guess

	$n_\alpha$	$n_\beta$	$n_\gamma$	$n_{vis}$
Gypsum	1.519–1.521	1.522–1.523	1.529–1.53	1.524
Bassanite	1.550–1.559	1.56	1.577–1.584	1.565

where  $\phi = 1$ -porosity, is the filling factor. When we take porosity into consideration, the Hapke's radiance coefficient (Equation 1) becomes to

$$REFF(i, e, g) = K \frac{w}{4} \frac{1}{\mu_0 + \mu} \left\{ [1 + B(g)]P(g) + H\left(\frac{\mu_0}{K}\right)H\left(\frac{\mu}{K}\right) - 1 \right\}. \quad (19)$$

Previous studies have shown that different values of porosity can change the value of  $k$  by a factor of two or more (Hapke, 2012; Sklute et al., 2015). Due to the uncertainty associated with porosity estimates, we tested the effect of different filling factors on the derived optical constants. It is clear to see from Figure 10 that the variations of  $k$  values from different porosity corrections are significant, while  $n$  values do not change at all, likely due to the dominance of the MIR  $k$  values on the Kramers–Kronig transformation. In the absence of precise knowledge of the packing density of each of these minerals at each grain size, we opted to not include porosity in the model for our calculations but provide the reader with both data and programs should they desire to reassess this common assumption.

#### 4.4. Comparison With Previous Results

Roush et al. (2007) and Robertson et al. (2016) have previously derived gypsum VNIR optical constants. Here we compare the gypsum VNIR optical constants derived from this work with those from the Hapke scattering model in Roush et al. (2007) and Robertson et al. (2016) (Figure 11). Robertson et al. (2016) and our work both find an optimized single array  $k$ -value for a range of particle sizes simultaneously, which is the main difference to the method of Roush et al. (2007). Robertson et al. (2016) calculated two types of optical constants of gypsum, for spherical particles and irregular particles. In their study, they related optical path length  $\langle D \rangle$  to the physical particle size  $D$  by  $\langle D \rangle \approx 0.9D$  for spherical particles and  $\langle D \rangle \approx 0.2D$  for irregular particles. Our work derived  $\langle D \rangle$  about  $1/3$  of the lower bound of size fraction which is close to the irregular particle case  $\langle D \rangle = 0.2D$  if we use the relationship as defined in Robertson et al. (2016). This result corresponds to the gypsum particle habit. However, the  $k$  values from this work show significant differences compared to the results of irregular particles in Robertson et al. (2016). Instead, our  $k$  values are nearly identical to the results of spherical particles in Robertson et al. (2016). The reason that our  $k$  values are close to that of spherical case in Robertson et al. (2016) is mainly because their prepared gypsum particles are smaller than samples in our study, and their spherical case for  $\langle D \rangle$  is on the same magnitude of

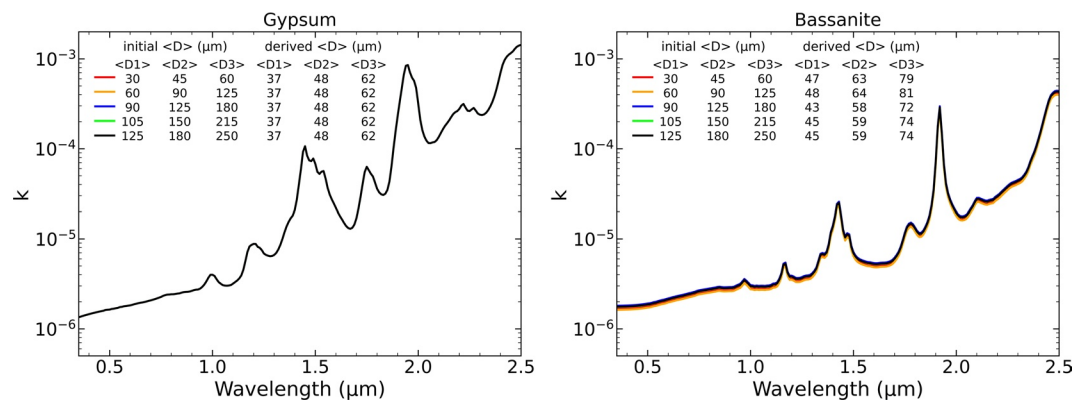


**Figure 8.** Derived visible/near-infrared imaginary refractive index of gypsum (left) and bassanite (right) from different initial guess of  $\langle D \rangle$  with reflectance data at one phase angle ( $i = 45^\circ$ ,  $e = -20^\circ$ ) and three grain sizes D1 = 90–125  $\mu\text{m}$ , D2 = 125–180  $\mu\text{m}$ , and D3 = 180–250  $\mu\text{m}$ .

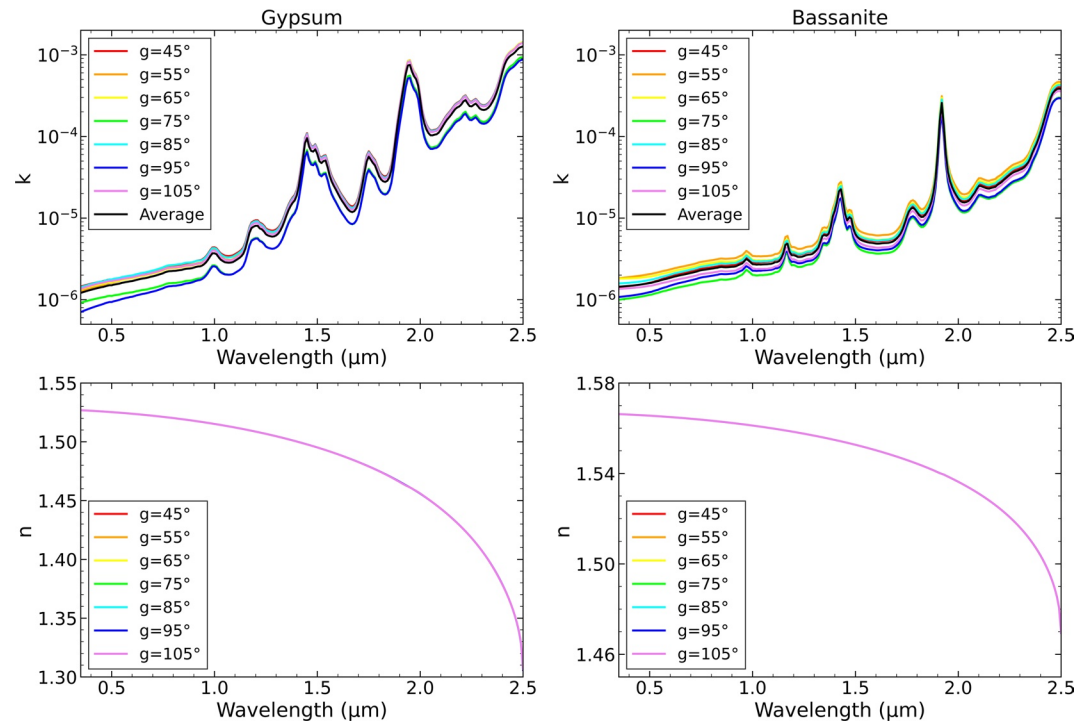


**Figure 9.** Derived visible/near-infrared optical constants of gypsum (left) and bassanite (right) from reflectance data at seven different phase angles.

ours. Although optical constants are grain size independent parameters in theory, the calculation of optical constants is mainly impacted by particle size. The difference between our results and previous studies are mainly caused by the different methods that are used to find the single array of  $k$ , as well as how the phase function and  $H$ -function are dealt with. As we discussed previously, this study used a global optimization to find a single array  $k$ -values instead of averaged  $k$  values from different particle sizes. We determined the wavelength dependent phase function from reflectance at multiple phase angles instead of assuming a constant phase function. We also used the extrapolation of Chandrasekhar's  $H$ -function table as  $H(x)$  rather than an approximation from Hapke (2012) because of the insufficient accuracy of the  $H(x)$  approximation when single scattering albedo is very close to 1. Our values for  $n$  drops off much more steeply toward longer wavelengths than those of Roush et al. (2007). This trend is the same seen by Sklute et al. (2015) and results from the different range of  $k$  values used to determine  $n$  through Kramers–Kronig analysis. In addition, since there is nearly two orders of magnitude difference in  $k$  values at the overlap region of VNIR and MIR data set, the way of combining MIR and VNIR  $k$ -values would affect the derived  $n$  values, resulting in different

**Table 3**

Final Values of Effective Grain Size  $\langle D \rangle$  ( $\mu\text{m}$ ), and Internal Scattering Coefficient  $s$  ( $\mu\text{m}^{-1}$ ) for Both Gypsum and Bassanite at 7 Phase Angles and Three Particle Size Fractions  $D1 = 90\text{--}125 \mu\text{m}$ ,  $D2 = 125\text{--}180 \mu\text{m}$ , and  $D3 = 180\text{--}250 \mu\text{m}$

Phase angle	Gypsum						Bassanite					
	$\langle D1 \rangle$	$\langle D2 \rangle$	$\langle D3 \rangle$	$s1$	$s2$	$s2$	$\langle D1 \rangle$	$\langle D2 \rangle$	$\langle D3 \rangle$	$s1$	$s2$	$s2$
$g = 45^\circ$	34	48	61	$10^{-4}$	0.1	0.1	49	66	83	0.1	0.005	0.1
$g = 55^\circ$	37	45	60	$10^{-7}$	0.1	0.1	42	56	71	$10^{-4}$	0.004	0.1
$g = 65^\circ$	37	48	62	$10^{-5}$	0.1	0.1	43	58	72	0.02	$10^{-7}$	0.1
$g = 75^\circ$	54	75	99	$10^{-14}$	0.1	0.1	65	90	112	0.1	$10^{-7}$	0.1
$g = 85^\circ$	36	48	60	$10^{-6}$	0.1	0.07	46	62	80	0.06	0.005	0.1
$g = 95^\circ$	57	77	106	$10^{-14}$	0.1	0.1	72	96	119	0.1	$10^{-8}$	0.1
$g = 105^\circ$	37	48	63	$10^{-6}$	0.1	0.1	53	72	90	0.003	$10^{-4}$	0.1

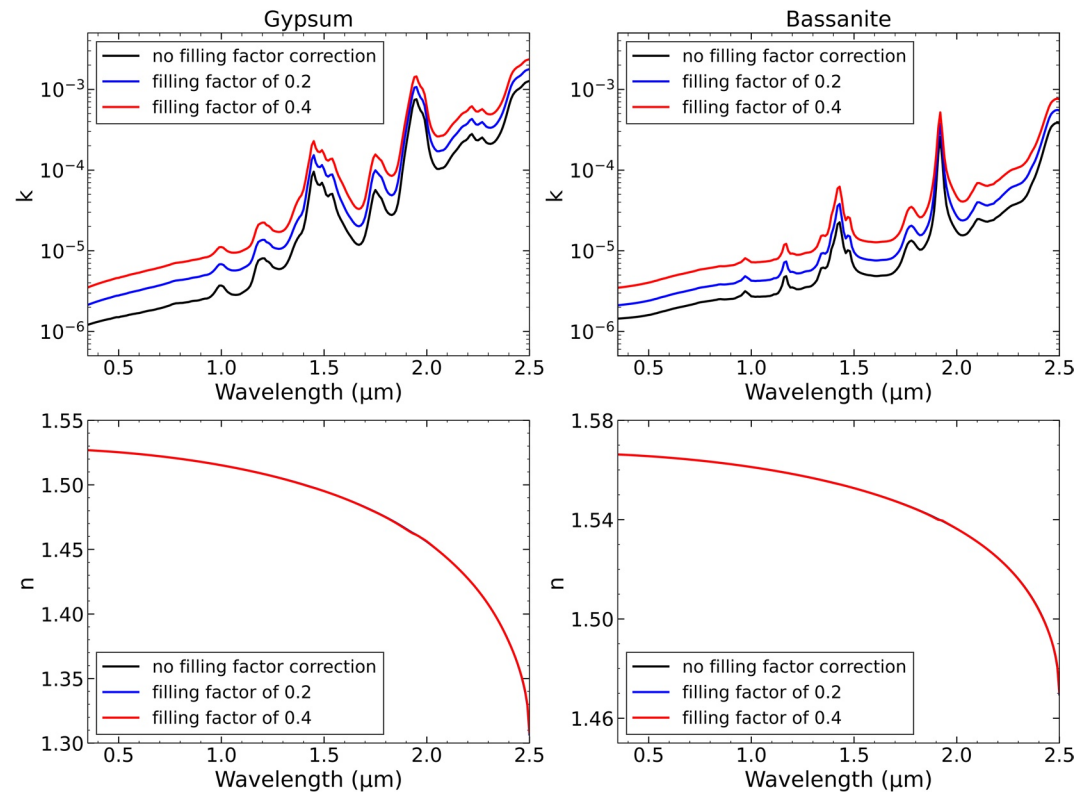


**Figure 10.** Derived visible/near-infrared optical constants for gypsum (left) and bassanite (right) from different porosity corrections.

slope curves of  $n$  in VNIR range (Ye et al., 2019). Therefore, it always requires a subjective adjustment to either MIR or VNIR data set for combining  $k$  values in these two wavelength ranges. In Figure 12, we compare the single scattering albedo of gypsum calculated with a constant  $n$  value as used in Robertson et al. (2016) and wavelength dependent  $n$  values as derived in this study while fixing other parameters. We can see that although the single scattering albedo are almost identical at the most wavelengths, the differences at the longer wavelengths are clearly caused by the different  $n$  values, which would have apparent effect on the spectral mixture modeling results. Overall, our results illustrate the need to use a wavelength dependent, rather than a constant  $n$  value in radiative transfer modeling, as  $n$  values of minerals can vary substantially over the VNIR wavelength range.

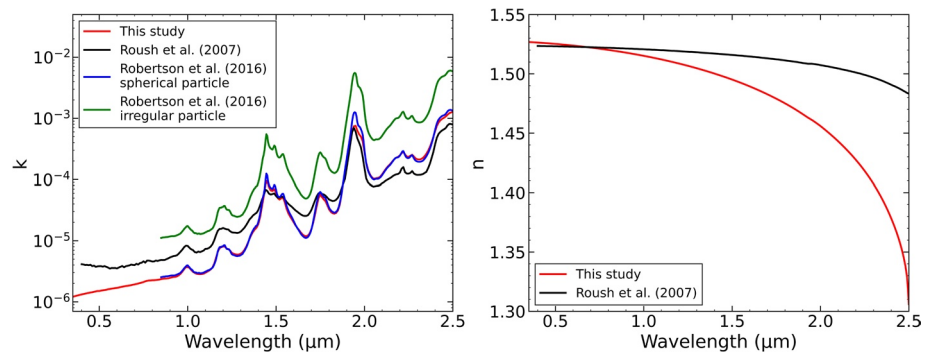


**Figure 11.** Comparison of gypsum V optical constants derived from this study, Roush et al. (2007) and Robertson et al. (2016). Robertson et al. (2016) used a constant value of  $n = 1.51$ . No porosity effect was considered in this comparison.

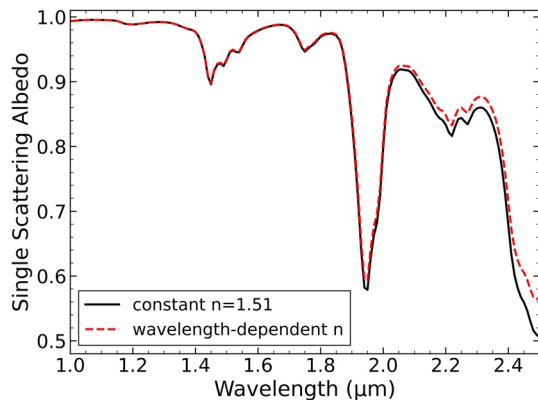


**Figure 12.** Comparison of single scattering albedo of gypsum calculated with a constant value of  $n = 1.51$  used in Robertson et al. (2016) and wavelength dependent  $n$  values derived in this study. The single scattering albedo is calculated through Equations 3–8, where  $k$  is taken from the result derived in this study,  $\langle D \rangle$  is set to  $62 \mu\text{m}$ , and  $s$  is set to 0.

#### 4.5. Potential Applications of Gypsum and Bassanite Optical Constants on Mars

The presence of various types of sulfates (Fe-, Mg-, and Ca-sulfates) have been detected in numerous regions of Mars from both orbital and in-situ observations. The extensive distribution of sulfate minerals in sedimentary deposits and soils has given rise to a conception that the Martian geological history has been dominated by a sulfur cycle in contrast to a carbon cycle on Earth (King & McLennan, 2010; McLennan, 2012). Optical constants of several hydrated Mg-sulfates (Dalton & Pitman, 2012) and Fe-sulfates (Pitman et al., 2014) have been studied previously. In this work, we focus on the optical constants derivation of Ca-sulfates, gypsum and bassanite, with the method developed by Sklute et al. (2021). We should note that the third kind of Ca-sulfate, anhydrite, has not been included in this study because it has no absorption features in the VNIR wavelength region.

The largest gypsum occurrence on Mars is located at the Olympia dunes in the north polar region (Langevin et al., 2005). Various formation mechanisms of gypsum in the north polar region of Mars have been proposed. Langevin et al. (2005) suggested that interaction of acidic snow with Ca-

rich minerals during volcanic activity or evaporation of the outflows from the melted ice cap would form gypsum deposits at the sand dunes in the Olympia Planitia. Fishbaugh et al. (2007) fitted the OMEGA spectra of gypsum at the Olympia Undae dune field with 35% pure gypsum of a few tens of microns in grain size mixed with 65% millimeter-sized gypsum containing dark, spectrally featureless materials. They hypothesized that these locally gypsum-rich dunes formed by in-situ weathering of sulfide and high-Ca-pyroxene dunes followed by evaporation in the pore spaces of these dunes after water from nearby channels percolated through them. Massé et al. (2010, 2012) identified spectroscopically weak signatures of gypsum sediment covering the surface of the north polar cap and the circum-polar dunes other than the restricted areas at the Olympia Undae. This wider distribution of gypsum deposits at the north polar region of Mars suggests that the polar gypsum was initially formed by acidic weathering of dust particles that were deposited in the ice, then released and transported by ice sublimation and winds (Massé et al., 2010, 2012). A similar scenario of glacial origin has been proposed for the formation of sulfate deposits at equatorial Meridiani Planum and Interior Layer Deposits (ILDs) in Valles Marineris during periods of high obliquity (Michalski & Niles, 2012; Niles & Michalski, 2009).

Gypsum located in layered deposits at lower latitudes has been reported for multiple regions (Gendrin et al., 2005; Sefton-Nash et al., 2012; Wray et al., 2011; Weitz et al., 2013, 2015). The appearance of sulfate deposits in the large-scale ILDs in equatorial areas has been suggested to originate from precipitation through evaporation, alteration by acidic groundwater circulation or volcanic outgassing (Gendrin et al., 2005), or sublimation of massive ice deposits consisting of dust and sulfur aerosols (Michalski & Niles, 2012). Wray et al. (2011) found a discrete ring of lighted-toned layered deposits including gypsum, Fe/Mg-sulfates, and phyllosilicates around the walls of Columbus crater in the Terra Sirenum, from which they hypothesized that the precipitation of sulfates came from a groundwater-fed deep lake. Gypsum associated with other hydrated minerals identified within a trough of Noctis Labyrinthus and bright layered mounds in the floor of Melas Chasma by Weitz et al. (2013, 2015) suggested that some localized aqueous activities could have occurred relatively late in Martian history.

Bassanite has been detected on the outflow channel floor at Mawrth Vallis by Wray et al. (2010). Surprisingly, bassanite was found underlying phyllosilicate-bearing layer deposits and seemed to predate the phyllosilicate unit, which was not consistent with the model proposed by Bibring et al. (2006) that sulfates usually formed later than phyllosilicates on Mars. The occurrence of bassanite at Mawrth Vallis could be explained by the leaching of Ca from upper layers followed by the precipitation of Ca-sulfate in the lower units, or might indicate a more complex Martian aqueous history than the theory of Bibring et al. (2006) suggested (Wray et al., 2010). The identification of hydrated minerals with the possible presence of bassanite in one chasma of the Noctis Labyrinthus region by Mangold et al. (2010) indicated a late-Amazonian

aqueous alteration process. The appearance of these phases with the close proximity of a volcanic plain suggested that bassanite may be formed by the interaction of local snow with hot volcanic ash or by the direct solid-gas interaction in relation to volcanic activity (Mangold et al., 2010).

The wide occurrence of a variety of chemically different sulfates on Mars displays a diverse degree of hydration states, which could indicate various sedimentary environments. While Ca-sulfates do not have a broad range of hydration states compared to Fe/Mg-sulfates, the distribution, stability, and relative abundance of hydrous sulfate salts on the Martian surface would provide significant constraints on their formation conditions and Martian hydrologic cycle. In this work, the optical constants of hydrous Ca-sulfates will be the addition to that of Fe/Mg-sulfates derived by Dalton and Pitman (2012) and Pitman et al. (2014). These optical constants data will facilitate mineral abundance extraction using radiative transfer models and increase the scientific return of remote sensing datasets.

## 5. Conclusion

The VNIR and MIR optical constants of gypsum and bassanite determined in this work expand the library of optical constants. With the availability of these optical constants, radiative transfer models can be used to estimate the individual component abundances of hydrous Ca-sulfates from the mineral mixtures. The  $k$ -values for gypsum at VNIR wavelengths show close agreements with results from Robertson et al. (2016) for a spherical particle assumption. In addition to the acquisition of optical constants, the wavelength dependent phase function has been constrained by reflectance from multiple phase angles. The combination of optical constants at MIR wavelengths allows us to derive the wavelength dependent  $n$  values with Kramers–Kronig analysis. Although  $n$  values do not change a lot at VNIR wavelengths, the derivation of absolute wavelength dependent  $n$  values, along with our refined  $k$ -values, could facilitate better accuracy in spectral unmixing of terrestrial and Martian remote sensing data sets that are expected to include hydrous Ca-sulfates.

## Data Availability Statement

Laboratory spectra and derived optical constants are archived at [Zenodo.org](https://doi.org/10.5281/zenodo.4735694) <https://doi.org/10.5281/zenodo.4735694>. The MATLAB code used to model the optical constants is available at [Zenodo.org](https://doi.org/10.5281/zenodo.4429127) <https://doi.org/10.5281/zenodo.4429127>.

## Acknowledgments

This work is supported by the RIS<sup>4</sup>E (Award NNA14B04A) and RISE2 (Award 80NSSC19M0215) nodes of NASA's Solar System Exploration Research Virtual Institute.

## References

- Adams, J. B. (1993). Imaging spectroscopy: Interpretation based on spectral mixture analysis. In C. M. Pieters, & P. A. Englert (Eds.), *Remote geochemical analysis: Elemental and mineralogical composition* (pp. 145–166): Cambridge University Press.
- Alpers, C. N., Jambor, J. L., & Nordstrom, D. (2000). *Sulfate minerals: Crystallography, geochemistry, and environmental significance*. Mineralogical Society of America.
- Anthony, J. W., Bideaux, R. A., Bladh, K. W., & Nichols, M. C. (1995). *Handbook of Mineralogy*. Mineral Data Publishing.
- Arnold, J. A., Glotch, T. D., & Plonka, A. M. (2014). Mid-infrared optical constants of clinopyroxene and orthoclase derived from oriented single-crystal reflectance spectra. *American Mineralogist*, 99(10), 1942–1955. <https://doi.org/10.2138/am-2014-4828>
- Aronson, J. R., Emslie, A. G., Miseso, E. V., Smith, E. M., & Strong, P. F. (1983). Optical constants of monoclinic anisotropic crystals: Gypsum. *Applied Optics*, 22(24), 4093–4098. <https://doi.org/10.1364/AO.22.004093>
- Aronson, J. R., Emslie, A. G., & Strong, P. F. (1985). Optical constants of triclinic anisotropic crystals: Blue vitriol. *Applied Optics*, 24(8), 1200–1203. <https://doi.org/10.1364/AO.24.001200>
- Bishop, J. L., Lane, M. D., Dyar, M. D., King, S. J., Brown, A. J., & Swayze, G. A. (2014). Spectral properties of Ca-sulfates: Gypsum, bassanite, and anhydrite. *American Mineralogist*, 99(10), 2105–2115. <https://doi.org/10.2138/am-2014-4756>
- Bibring, J.-P., Langevin, Y., Mustard, J. F., Poulet, F., Arvidson, R., Gendrin, A., et al. (2006). Global mineralogical and aqueous Mars history derived from OMEGA/Mars express data. *Science*, 312(5772), 400–404. <https://doi.org/10.1126/science.1122659>
- Chandrasekhar, S. (1960). *Radiative transfer*. New York: Dover Publications.
- Cloutis, E. A., Craig, M. A., Kruzelecky, R. V., Jamroz, W. R., Scott, A., Hawthorne, F. C., & Mertzman, S. A. (2008). Spectral reflectance properties of minerals exposed to simulated Mars surface conditions. *Icarus*, 195(1), 140–168. <https://doi.org/10.1016/j.icarus.2007.10.028>
- Cloutis, E. A., Hawthorne, F. C., Mertzman, S. A., Krenn, K., Craig, M. A., Marcino, D., et al. (2006). Detection and discrimination of sulfate minerals using reflectance spectroscopy. *Icarus*, 184(1), 121–157. <https://doi.org/10.1016/j.icarus.2006.04.003>
- Cord, A. M., Pinet, P. C., Daydou, Y., & Chevrel, S. D. (2003). Planetary regolith surface analogs: Optimized determination of Hapke parameters using multi-angular spectro-imaging laboratory data. *Icarus*, 165(2), 414–427. [https://doi.org/10.1016/S0019-1035\(03\)00204-5](https://doi.org/10.1016/S0019-1035(03)00204-5)
- Crowley, J. K. (1991). Visible and near-infrared (0.4–2.5  $\mu\text{m}$ ) reflectance spectra of Playa evaporite minerals. *Journal of Geophysical Research*, 96(B10), 16231–16240. <https://doi.org/10.1029/91JB01714>
- Dalton, J. B., & Pitman, K. M. (2012). Low temperature optical constants of some hydrated sulfates relevant to planetary surfaces. *Journal of Geophysical Research*, 117(E9). <https://doi.org/10.1029/2011JE004036>

- Fishbaugh, K. E., Poulet, F., Chevrier, V., Langevin, Y., & Bibring, J.-P. (2007). On the origin of gypsum in the Mars north polar region. *Journal of Geophysical Research*, *112*(E7). <https://doi.org/10.1029/2006JE002862>
- Gendrin, A., Mangold, N., Bibring, J.-P., Langevin, Y., Gondet, B., Poulet, F., et al. (2005). Sulfates in Martian layered terrains: The OMEGA/Mars Express View. *Science*, *307*(5715), 1587–1591. <https://doi.org/10.1126/science.1109087>
- Gillespie, A. R. (1992). Spectral mixture analysis of multispectral thermal infrared images. *Remote Sensing of Environment*, *42*(2), 137–145. [https://doi.org/10.1016/0034-4257\(92\)90097-4](https://doi.org/10.1016/0034-4257(92)90097-4)
- Glotch, T. D., & Rossman, G. R. (2009). Mid-infrared reflectance spectra and optical constants of six iron oxide/oxyhydroxide phases. *Icarus*, *204*(2), 663–671. <https://doi.org/10.1016/j.icarus.2009.07.024>
- Glotch, T. D., Rossman, G. R., & Aharonson, O. (2007). Mid-infrared (5–100  $\mu\text{m}$ ) reflectance spectra and optical constants of ten phyllosilicate minerals. *Icarus*, *192*(2), 605–622. <https://doi.org/10.1016/j.icarus.2007.07.002>
- Hapke, B. (1981). Bidirectional reflectance spectroscopy: 1. Theory. *Journal of Geophysical Research*, *86*(B4), 3039–3054. <https://doi.org/10.1029/JB086iB04p03039>
- Hapke, B. (2001). Space weathering from Mercury to the asteroid belt. *Journal of Geophysical Research*, *106*(E5), 10039–10073. <https://doi.org/10.1029/2000JE001338>
- Hapke, B. (2008). Bidirectional reflectance spectroscopy: 6. Effects of porosity. *Icarus*, *195*(2), 918–926. <https://doi.org/10.1016/j.icarus.2008.01.003>
- Hapke, B. (2012). Bidirectional reflectance spectroscopy: 7. The single particle phase function hockey stick relation. *Icarus*, *221*(2), 1079–1083. <https://doi.org/10.1016/j.icarus.2012.10.022>
- Hapke, B., & Wells, E. (1981). Bidirectional reflectance spectroscopy: 2. Experiments and observations. *Journal of Geophysical Research*, *86*(B4), 3055–3060. <https://doi.org/10.1029/JB086iB04p03055>
- Harrison, T. N. (2012). Experimental VNIR reflectance spectroscopy of gypsum dehydration: Investigating the gypsum to bassanite transition. *American Mineralogist*, *97*(4), 598–609. <https://doi.org/10.2138/am.2012.3667>
- Hartman, B., & Domingue, D. (1998). Scattering of light by individual particles and the implications for models of planetary surfaces. *Icarus*, *131*(2), 421–448. <https://doi.org/10.1006/icar.1997.5861>
- Harvie, C. E., Møller, N., & Weare, J. H. (1984). The prediction of mineral solubilities in natural waters: The Na-K-Mg-Ca-H-Cl-SO<sub>4</sub>-OH-HCO<sub>3</sub>-CO<sub>3</sub>-CO<sub>2</sub>-H<sub>2</sub>O system to high ionic strengths at 25°C. *Geochimica et Cosmochimica Acta*, *48*(4), 723–751. [https://doi.org/10.1016/0016-7037\(84\)90098-X](https://doi.org/10.1016/0016-7037(84)90098-X)
- Hunt, G. R. (1977). Spectral signatures of particulate minerals in the visible and near infrared. *Geophysics*, *42*(3), 501–513. <https://doi.org/10.1190/1.1440721>
- King, P. L., & McLennan, S. M. (2010). Sulfur on Mars. *Elements*, *6*(2), 107–112. <https://doi.org/10.2113/gselements.6.2.107>
- Langevin, Y., Poulet, F., Bibring, J.-P., & Gondet, B. (2005). Sulfates in the North Polar region of Mars detected by OMEGA/Mars Express. *Science*, *307*(5715), 1584–1586. <https://doi.org/10.1126/science.1109091>
- L'Haridon, J., Mangold, N., Meslin, P.-Y., Johnson, J. R., Rapin, W., Forni, O., et al. (2018). Chemical variability in mineralized veins observed by ChemCam on the lower slopes of Mount Sharp in Gale crater, Mars. *Icarus*, *311*, 69–86. <https://doi.org/10.1016/j.icarus.2018.01.028>
- Lucarini, V., Saarinen, J. J., Peiponen, K.-E., & Vartiainen, E. M. (2005). *Kramers–Kronig relations in optical materials Research*. Springer Science & Business Media.
- Lucey, P. G. (1998). Model near-infrared optical constants of olivine and pyroxene as a function of iron content. *Journal of Geophysical Research*, *103*(E1), 1703–1713. <https://doi.org/10.1029/97JE03145>
- Mangold, N., Roach, L., Milliken, R., Le Mouélic, S., Ansan, V., Bibring, J. P., et al. (2010). A late Amazonian alteration layer related to local volcanism on Mars. *Icarus*, *207*(1), 265–276. <https://doi.org/10.1016/j.icarus.2009.10.015>
- Massé, M., Bourgeois, O., Le Mouélic, S., Verpoorter, C., Le Deit, L., & Bibring, J. P. (2010). Martian polar and circum-polar sulfate-bearing deposits: Sublimation tills derived from the North Polar Cap. *Icarus*, *209*(2), 434–451. <https://doi.org/10.1016/j.icarus.2010.04.017>
- Massé, M., Bourgeois, O., Le Mouélic, S., Verpoorter, C., Spiga, A., & Le Deit, L. (2012). Wide distribution and glacial origin of polar gypsum on Mars. *Earth and Planetary Science Letters*, *317*–*318*, 44–55. <https://doi.org/10.1016/j.epsl.2011.11.035>
- Mayerhöfer, T. G., & Popp, J. (2007). Employing spectra of polycrystalline materials for the verification of optical constants obtained from corresponding low-symmetry single crystals. *Applied Optics*, *46*(3), 327–334. <https://doi.org/10.1364/AO.46.000327>
- McGuire, A. F., & Hapke, B. W. (1995). An experimental study of light scattering by large, irregular particles. *Icarus*, *113*(1), 134–155. <https://doi.org/10.1006/icar.1995.1012>
- McLennan, S. M. (2012). Geochemistry of sedimentary processes on Mars. *Sedimentary Geology of Mars*, *102*, 119–138. <https://doi.org/10.2110/pec.12.102.0119>
- Mees, F. (1998). The alteration of glauberite in lacustrine deposits of the Taoudenni-Agorgott basin, northern Mali. *Sedimentary Geology*, *117*(3), 193–205. [https://doi.org/10.1016/S0037-0738\(98\)00042-6](https://doi.org/10.1016/S0037-0738(98)00042-6)
- Michalski, J., & Niles, P. B. (2012). Atmospheric origin of Martian interior layered deposits: Links to climate change and the global sulfur cycle. *Geology*, *40*(5), 419–422. <https://doi.org/10.1130/G32971.1>
- Mustard, J. F., & Pieters, C. M. (1989). Photometric phase functions of common geologic minerals and applications to quantitative analysis of mineral mixture reflectance spectra. *Journal of Geophysical Research*, *94*(B10), 13619–13634. <https://doi.org/10.1029/JB094iB10p13619>
- Nachon, M., Clegg, S. M., Mangold, N., Schröder, S., Kah, L. C., Dromart, G., et al. (2014). Calcium sulfate veins characterized by ChemCam/Curiosity at Gale crater, Mars. *Journal of Geophysical Research: Planets*, *119*(9), 1991–2016. <https://doi.org/10.1002/2013JE004588>
- Nachon, M., Mangold, N., Forni, O., Kah, L. C., Cousin, A., Wiens, R. C., et al. (2017). Chemistry of diagenetic features analyzed by ChemCam at Pahrump Hills, Gale crater, Mars. *Icarus*, *281*, 121–136. <https://doi.org/10.1016/j.icarus.2016.08.026>
- Niles, P. B., & Michalski, J. (2009). Meridiani Planum sediments on Mars formed through weathering in massive ice deposits. *Nature Geoscience*, *2*(3), 215–220. <https://doi.org/10.1038/ngeo438>
- Ossorio, M., Van Driessche, A. E. S., Pérez, P., & García-Ruiz, J. M. (2014). The gypsum–anhydrite paradox revisited. *Chemical Geology*, *386*, 16–21. <https://doi.org/10.1016/j.chemgeo.2014.07.026>
- Pieters, C. M., Fischer, E. M., Rode, O., & Basu, A. (1993). Optical effects of space weathering: The role of the finest fraction. *Journal of Geophysical Research*, *98*(E11), 20817–20824. <https://doi.org/10.1029/93JE02467>
- Pitman, K. M., Dobrea, E. Z. N., Jamieson, C. S., Dalton, J. B., Abbey, W. J., & Joseph, E. C. S. (2014). Reflectance spectroscopy and optical functions for hydrated Fe-sulfates. *American Mineralogist*, *99*(8–9), 1593–1603. <https://doi.org/10.2138/am.2014.4730>
- Rampe, E. B., Ming, D. W., Blake, D. F., Bristow, T. F., Chipera, S. J., Grotzinger, J. P., et al. (2017). Mineralogy of an ancient lacustrine mudstone succession from the Murray formation, Gale crater, Mars. *Earth and Planetary Science Letters*, *471*, 172–185. <https://doi.org/10.1016/j.epsl.2017.04.021>

- Ramsey, M. S., & Christensen, P. R. (1998). Mineral abundance determination: Quantitative deconvolution of thermal emission spectra. *Journal of Geophysical Research*, 103(B1), 577–596. <https://doi.org/10.1029/97JB02784>
- Rapin, W., Meslin, P.-Y., Maurice, S., Vaniman, D., Nachon, M., Mangold, N., et al. (2016). Hydration state of calcium sulfates in Gale crater, Mars: Identification of bassanite veins. *Earth and Planetary Science Letters*, 452, 197–205. <https://doi.org/10.1016/j.epsl.2016.07.045>
- Robertson, K., & Bish, D. (2013). Constraints on the distribution of  $\text{CaSO}_4 \cdot n\text{H}_2\text{O}$  phases on Mars and implications for their contribution to the hydrological cycle. *Icarus*, 223(1), 407–417. <https://doi.org/10.1016/j.icarus.2012.10.028>
- Robertson, K. M., Milliken, R. E., & Li, S. (2016). Estimating mineral abundances of clay and gypsum mixtures using radiative transfer models applied to visible-near infrared reflectance spectra. *Icarus*, 277, 171–186. <https://doi.org/10.1016/j.icarus.2016.04.034>
- Roush, T., Pollack, J., & Orenberg, J. (1991). Derivation of midinfrared (5–25  $\mu\text{m}$ ) optical constants of some silicates and palagonite. *Icarus*, 94(1), 191–208. [https://doi.org/10.1016/0019-1035\(91\)90150-R](https://doi.org/10.1016/0019-1035(91)90150-R)
- Roush, T. L. (1995). Optical constants of amorphous carbon in the mid-IR (2.5–25  $\mu\text{m}$ , 4000–400  $\text{cm}^{-1}$ ). *Planetary and Space Science*, 43(10), 1297–1301. [https://doi.org/10.1016/0032-0633\(95\)00008-S](https://doi.org/10.1016/0032-0633(95)00008-S)
- Roush, T. L. (1996). Midinfrared (5.0 – 25  $\mu\text{m}$ , 2000 – 400  $\text{cm}^{-1}$ ) optical constants of hydrous carbonate, sulfate, and nitrate. *Journal of Geophysical Research*, 101(E1), 2215–2224. <https://doi.org/10.1029/95JE03364>
- Roush, T. L. (2003). Estimated optical constants of the Tagish Lake meteorite. *Meteoritics & Planetary Science*, 38(3), 419–426. <https://doi.org/10.1111/j.1945-5100.2003.tb00277.x>
- Roush, T. L. (2005). Near-infrared (0.67–4.7  $\mu\text{m}$ ) optical constants estimated for montmorillonite. *Icarus*, 179(1), 259–264. <https://doi.org/10.1016/j.icarus.2005.06.004>
- Roush, T. L. (2021). Estimation of visible, near-, and mid-infrared complex refractive indices of calcite, dolomite, and magnesite. *Icarus*, 354, 114056. <https://doi.org/10.1016/j.icarus.2020.114056>
- Roush, T. L., Esposito, F., Rossman, G. R., & Colangeli, L. (2007). Estimated optical constants of gypsum in the regions of weak absorptions: Application of scattering theories and comparisons to independent measurements. *Journal of Geophysical Research*, 112(E10). <https://doi.org/10.1029/2007JE002920>
- Sefton-Nash, E., Catling, D. C., Wood, S. E., Grindrod, P. M., & Teanby, N. A. (2012). Topographic, spectral and thermal inertia analysis of interior layered deposits in Iani Chaos, Mars. *Icarus*, 221(1), 20–42. <https://doi.org/10.1016/j.icarus.2012.06.036>
- Shepard, M. K., & Helfenstein, P. (2007). A test of the Hapke photometric model. *Journal of Geophysical Research*, 112(E3). <https://doi.org/10.1029/2005JE002625>
- Shkuratov, Y., Starukhina, L., Hoffmann, H., & Arnold, G. (1999). A model of spectral albedo of particulate surfaces: Implications for optical properties of the Moon. *Icarus*, 137(2), 235–246. <https://doi.org/10.1006/icar.1998.6035>
- Sklute, E. C., Domingue-Loren, D., Glotch, T. D., Rucks, M. J., & Ye, C. (2021). A new open-source Hapke radiative transfer program for determining optical constants and analyzing phase behavior. *Lunar and Planetary Science Conference*, 52: abstract 1258.
- Sklute, E. C., Glotch, T. D., Piatek, J. L., Woerner, W. R., Martone, A. A., & Kraner, M. L. (2015). Optical constants of synthetic potassium, sodium, and hydronium jarosite. *American Mineralogist*, 100(5–6), 1110–1122. <https://doi.org/10.2138/am-2015-4824>
- Spitzer, W. G., & Kleinman, D. A. (1961). Infrared lattice bands of quartz. *Physical Review*, 121(5), 1324–1335. <https://doi.org/10.1103/PhysRev.121.1324>
- Squyres, S. W., Arvidson, R. E., Bell, J. F., Calef, F., Clark, B. C., Cohen, B. A., et al. (2012). Ancient impact and aqueous processes at endeavour crater, Mars. *Science*, 336(6081), 570–576. <https://doi.org/10.1126/science.1220476>
- Vaniman, D. T., Martínez, G. M., Rampe, E. B., Bristow, T. F., Blake, D. F., Yen, A. S., et al. (2018). Gypsum, bassanite, and anhydrite at Gale crater, Mars. *American Mineralogist*, 103(7), 1011–1020. <https://doi.org/10.2138/am-2018-6346>
- Weitz, C. M., Bishop, J. L., & Grant, J. A. (2013). Gypsum, opal, and fluvial channels within a trough of Noctis Labyrinthus, Mars: Implications for aqueous activity during the Late Hesperian to Amazonian. *Planetary and Space Science*, 87, 130–145. <https://doi.org/10.1016/j.pss.2013.08.007>
- Weitz, C. M., Dobre, E. N., Wray, J. J. (2015). Mixtures of clays and sulfates within deposits in western Melas Chasma, Mars. *Icarus*, 251, 291–314. <https://doi.org/10.1016/j.icarus.2014.04.009>
- Wray, J. J., Milliken, R. E., Dundas, C. M., Swayze, G. A., Andrews-Hanna, J. C., Baldridge, A. M., et al. (2011). Columbus crater and other possible groundwater-fed paleolakes of Terra Sirenum, Mars. *Journal of Geophysical Research*, 116, E01001. <https://doi.org/10.1029/2010JE003694>
- Wray, J. J., Squyres, S. W., Roach, L. H., Bishop, J. L., Mustard, J. F., & Noe Dobre, E. Z. (2010). Identification of the Ca-sulfate bassanite in Mawrth Vallis, Mars. *Icarus*, 209(2), 416–421. <https://doi.org/10.1016/j.icarus.2010.06.001>
- Yang, Y., Li, S., Milliken, R. E., Zhang, H., Robertson, K., & Hiroi, T. (2019). Phase functions of typical lunar surface minerals derived for the Hapke model and implications for visible to near-infrared spectral unmixing. *Journal of Geophysical Research: Planets*, 124(1), 31–60. <https://doi.org/10.1029/2018JE005713>
- Ye, C., Rucks, M. J., Arnold, J. A., & Glotch, T. D. (2019). Mid-infrared optical constants of labradorite, a triclinic plagioclase mineral. *Earth and Space Science*, 6(12), 2410–2422. <https://doi.org/10.1029/2019EA000915>
- Ye, C., Sklute, E. C., & Glotch, T. D. (2019). *Mind the Gap: Methods for combining optical constants from visible to infrared in the Kramers-Kronig analysis associated with Hapke modeling*: Lunar and Planetary Science Conference.